Time–dependent alignment of molecules
trapped in octahedral crystal fields

Toni Kiljunen,[1,2,*] Burkhard Schmidt,[3] and Nikolaus Schwentner[2]

[1]*Department of Chemistry, P.O. Box 35,*

FIN–40014 University of Jyväskylä, Finland

[2]*Institut für Experimentalphysik, Freie Universität Berlin,*

Arnimallee 14, D–14195 Berlin, Germany

[3]*Institut für Mathematik II, Freie Universität Berlin,*

Arnimallee 2–6, D–14195 Berlin, Germany

(Dated: January 20, 2006)

Abstract

The hindered rotational states of molecules confined in crystal fields of octahedral symmetry, and their time-dependent alignment obtained by pulsed nonresonant laser fields, are studied computationally. The control over the molecular axis direction is discussed based on the evolution of the rotational wave packet generated in the cubic crystal-field potential. The alignment degree obtained in a cooperative case, where the alignment field is applied in a favorable crystal-field direction, or in a competitive direction, where the crystal field has a saddle point, is presented. The investigation is divided into two time regimes where the pulse duration is either ultrashort, leading to nonadiabatic dynamics, or long with respect to period of molecular libration, which leads to synchronous alignment due to nearly adiabatic following. The results are contrasted to existing gas phase studies. The use of nonadiabatic alignment for interrogation of crystal-field energetics and the use of adiabatic alignment for directional control of molecular dynamics in solids are proposed as practical applications.

---

*E-mail: toni.kiljunen@jyu.fi

I. INTRODUCTION

The concept of alignment of neutral gas phase molecules along the polarization directions of laser pulses has reached a relatively mature state. Recent reviews exemplify the wide range of experimental and theoretical activity on that topic [1, 2] showing that robust and efficient manipulation of molecular alignment is based on the interaction of the anisotropic molecular polarizability with intense nonresonant laser fields [3, 4, 5]. During the past few years the original concept for linear molecules interacting with linearly polarized fields has been generalized [6, 7]. Currently three-dimensional alignment of more general molecules can be achieved by means of elliptically polarized laser fields [8].

When considering the time-dependent picture of molecular alignment, the underlying photoinduced rotational dynamics lies between the following two extremes: In the adiabatic case, which can be realized by light pulses long compared to the rotational period of the molecule, alignment can only be achieved while the field is turned on [1]. In contrast, field-free alignment is achieved in the nonadiabatic case, i. e., where the pulses are short compared with the rotational time scale [2]. The rotational wave packet states formed can be considered as coherent superpositions of field-free states and the post-pulse evolution is dominated by quantum beats and rotational revivals, see e. g., the combined theoretical and experimental studies of the nonadiabatic alignment of asymmetric [9] and symmetric [10] top molecules, and the seminal work in Refs. [11, 12, 13]. Different polarizations of the field have been exploited to further control the time-dependent alignment beyond the one-dimensional case [2, 8, 14, 15]. Also the use of suitably tailored combinations of pulses for enhancing the alignment has been investigated [16, 17, 18, 19, 20]. In other work, the concept is extended to include the influence of dissipative environments that lead to decoherence [21, 22] of the rotational densities.

For a molecule embedded in a crystalline solid, e. g., a small diatomic in a rare gas matrix [23], the fundamental difference to the gas-phase case stems from the internal field, often referred to as crystal field. In the absence of external fields, the densities tend to be angularly confined along the energetically preferred directions in the solid. Hence, for increasing crystal field, the free-rotor states become more and more hindered and are eventually transformed into librational states which are characterized by small-amplitude vibrational motion in the angular degrees of freedom. The corresponding energy levels arrange into near degenerate

multiplets that we shall designate as librational manifolds. As long as the energies are lower than the barrier heights, the dynamics within each of these manifolds is prevailed by the tunneling effect [24]. Typically, for small diatomic molecules trapped in rare-gas matrices, the librational and tunneling energy splittings (in units of the rotational constant B) are of the order of 10 and 0.1, respectively [25]. Consequently, when considering thermal ensembles, we shall distinguish three different temperature regimes in the following. For an ultra-low temperature $\mathcal{T} \approx 0.1$ (in reduced units k_B/B), only the ground state is populated despite the small energy gap to other tunneling states. In strong crystal fields the set of tunneling states is not separable by temperature due to the near degeneracy. In that librational limit, the situation resembles a low-temperature case $\mathcal{T} \approx 1$, where all the states within the multiplet are almost equally populated. Finally, for a high temperature $\mathcal{T} \approx 10$, many librational manifolds become populated.

The goal of alignment (and orientation) of molecules confined in matrices is to manipulate the directional properties of rotational densities with respect to crystallographic axes of the host lattice. In our previous work, the combined effect of (internal) octahedral potential and (external) light field on the alignment of linear molecules is investigated [26, 27]. It has been found that the resulting degree of alignment crucially depends on the relative orientation of the crystallographic axes and the polarization direction of the external field. If the direction of the external field coincides with minima of the crystal field, a high (near unity) alignment can be achieved for specific states, even for low field strengths and high temperatures. Otherwise, high efficiency of these mechanisms is restricted to high fields and low temperatures. The present work extends the previous studies of alignment from the frequency/energy domain into the time domain. To this end, we investigate the rotational dynamics by numerically solving the time-dependent Schrödinger equation for the angular degrees of freedom of a translationally caged molecule interacting with a nonresonant laser pulse of varying pulse length σ (FWHM in units of rotational period $h/2B$ of the $J = 0$ state). In analogy to the energy and temperature scales introduced above, we shall consider the following three cases: (1) In the (nearly sudden) limit of ultrashort pulses, $\sigma \approx 0.01$, a rotational wave packet is created which is a coherent superposition of several librational manifolds. (2) For a short pulse, $\sigma \approx 0.1$, only states within a single manifold are populated during the pulse. The first and second case shall be termed nonadiabatic with respect to librational and tunneling dynamics, respectively. In both these cases transient alignment

signals, $\langle \cos^2 \theta \rangle$, are to be analyzed. In particular, it shall be demonstrated how the quantum beats and revival structures can be used to reveal the underlying energy-level spacings which are inversely proportional to the temporal beatings of the field-free states comprising the wave packet [12, 13, 28]. This allows to deduce information about the crystal field itself which is usually not known *a priori*. (3) Finally, the case of long pulses, $\sigma \approx 1$, can be used to create a directionally anisotropic sample transiently during the pulse. Here we show that the adiabatic alignment serves to provide a suitable precondition for controlling subsequent photoinduced physics and chemistry in the solid. One can affect, e. g., vibrational wave-packet dynamics induced by pump-probe electronic excitation schemes [29, 30, 31]. In the present work we concentrate on a thermal ensemble at low temperature, $\mathcal{T} = 1$, where initially only the lowest librational manifold is essentially populated. Each of the six tunneling states in the set either end up with a coherent superposition of states (cases 1 and 2) that can be coupled by the field in multiple transition cycles, or evolve as a directional hybrid eigenstate (case 3). Different selection rules play a crucial role in determining the wave-packet composition.

II. COMPUTATIONAL METHOD

As a model system we consider a molecule in an electronically nondegenerate $^1\Sigma$ state. The cubic crystal field constrains its translational degrees of freedom to a site of octahedral symmetry while its rotational motion is moderately hindered, but not completely restricted, by the surroundings. This is often realized for diatomic impurities which are small enough to fit in a monosubstitutional lattice site [25]. As described before in Refs. [26, 27] and justified therein, we assume the molecular center of mass (c.m.) to be fixed at a substitutional lattice site. Moreover, the center of interaction (c.i.) is assumed to coincide with the c.m., and an additional eccentric motion about a separate c.i. can be accounted for by an effective (reduced) rotational constant $B = \hbar^2/2I$. Any deformations of the matrix in accommodating the impurity and in responding to impurity motions are neglected as we concentrate solely on the guest angular dynamics. Furthermore, we neglect any interaction between the laser field and the surrounding matrix.

The confined molecule has polarizability components parallel ($\alpha_\parallel$) and perpendicular ($\alpha_\perp$) to the molecular axis. It is subject to an intense nonresonant laser field $\mathcal{E}(t)$. The linear

4

polarization direction of the field is along either one of the $\langle 100 \rangle$ or $\langle 110 \rangle$ crystallographic axes. The interaction then depends on the polar angle θ between the molecular axis and the field direction defining the laboratory frame (Ω), and on the orientation with respect to the solid cage frame (Ω'). For the $\langle 100 \rangle$ direction of the field, we have coinciding axes systems $\theta' = \theta, \phi' = \phi$ whereas for $\langle 110 \rangle$ the relations are $\theta' = \theta - \pi/2, \phi' = \phi - \pi/4$.

We write the time-dependent Hamiltonian for the embedded molecule as

$$\hat{H}/B = (\hat{\mathbf{J}}/\hbar)^2 + \hat{V}_\kappa + \hat{V}_\alpha \,, \tag{1}$$

where $\hat{\mathbf{J}}$ is the angular momentum operator having its origin at the c.m. of the guest molecule. We present the static octahedral potential (crystal field) due to the solid surrounding as [27]

$$V_\kappa(\theta', \phi'; \kappa) = \kappa \left[-\frac{52}{11}\sqrt{\frac{\pi}{21}} V_4(\theta', \phi') + \frac{16}{11}\sqrt{\frac{\pi}{26}} V_6(\theta', \phi') \right] \,, \tag{2}$$

where κ is a dimensionless strength parameter (in units of B) and the angular functions $V_4(\theta', \phi')$ and $V_6(\theta', \phi')$ are the two lowest nontrivial surface harmonics which transform according to the A_{1g} representation of the O_h point group [32, 33, 34, 35]. The time dependence of the alignment field squared,

$$\mathcal{E}^2(\tau) = \frac{2\mathcal{I}_0}{c\epsilon} g(\tau) \cos^2(2\pi\nu\tau) \,, \tag{3}$$

is expressed in terms of its intensity envelope function $g(\tau)$, and the constants c and ϵ are the phase velocity of light and electronic permeability, respectively, in the homogeneous medium. Note that the oscillation frequency ν is assumed far from any molecular resonances and can be averaged out. The pulse shape is assumed to be of the form

$$g(\tau) = \exp[-4\ln(2)\tau^2/\sigma^2] \,.$$

Hence, the laser pulses are characterized by the duration σ (full width at half maximum, FWHM) given in reduced units of time, $\tau = 2tB/h$. The dimensionless intensity is

$$\Delta\omega = \frac{\Delta\alpha}{4B} \frac{2\mathcal{I}_0}{c\epsilon} = \frac{\Delta\alpha\mathcal{E}_0^2}{4B} \,,$$

with $\Delta\alpha = \alpha_\parallel - \alpha_\perp$. The molecule–laser interaction leads to an effective potential of the form

$$V_\alpha(\theta; \Delta\omega, \tau) = -(\Delta\omega \cos^2\theta + \omega_\perp)g(\tau) \,. \tag{4}$$

5

The present work is divided into investigations of rotational dynamics induced by (ultra)short and long pulses, according to the pulse width σ with respect to the rotational period of the free molecule $t_{\mathrm{rot}} = h/2B$, i. e., $\tau = 1$. In the former, nonadiabatic case the duration samples a range below t_{rot}, $\sigma = (0.01\text{--}0.5)/\pi$, whereas for the long pulse, adiabatic limit we consider pulse widths $\sigma = 0.5\text{--}4$.

The time-dependent Schrödinger equation corresponding to Eq. (1) is solved in spherical harmonics basis $\{Y_{J,M}(\theta, \phi)\}$ truncated at $J_{\max} = 16$. For each irreducible representation of the point groups involved, symmetry-adapted basis functions tabulated in Refs. [35, 36] have been used. In terms of the rotational density operator,

$$\hat{\rho}(\tau) = \sum_n w_n \hat{\rho}_n(\tau) = \sum_n w_n |\Psi_n(\tau)\rangle\langle\Psi_n(\tau)|, \tag{5}$$

the signal function, i. e., the time-dependent degree of alignment is represented by the expectation value

$$\langle\langle\cos^2\theta\rangle\rangle(\tau) = \mathrm{Tr}\{\hat{\rho}(\tau)\cos^2\theta\}, \tag{6}$$

where the double brackets indicate averaging over a thermal ensemble with Boltzmann weights $w_n = \exp(-E_n/\mathcal{T})/\sum_{n'}\exp(-E_{n'}/\mathcal{T})$. We restrict ourselves to a case of low reduced rotational temperature $\mathcal{T} = 1\ k_B/B$ which limits the initial population to the lowest manifold of librational states. The conversions of several quantities to practical units are: $\mathcal{I}_0[\mathrm{W\,cm^{-2}}] = \Delta\omega B[\mathrm{cm^{-1}}]/(1.055 \times 10^{-11}\Delta\alpha[\mathrm{\mathring{A}}^3])$ for the field intensity, $t[\mathrm{ps}] = 16.68\tau/B[\mathrm{cm^{-1}}]$ for time, and $T[\mathrm{K}] = 1.44\mathcal{T}B[\mathrm{cm^{-1}}]$ for temperature. Note also that the energies E_n presented are always given in units of B.

III. TIME–INDEPENDENT STATES

A. Crystal–field states

We use the same form of the octahedral crystal-field potential in Eq. (2) as in Ref. [27], where its properties were described in detail. In particular, the potential has a sixfold set of symmetry equivalent minima in the $\langle 100\rangle$ directions with energies $V_\kappa/\kappa = -1$. Twelve equivalent saddle points (barriers between the minima) have zero energy, independent of κ, in the $\langle 110\rangle$ directions, and an eightfold set of maxima with $V_\kappa/\kappa = 10/9$ is found for the $\langle 111\rangle$ directions. In our previous work, we have characterized how the internal crystal

field affects the angular degrees of freedom of molecules trapped in octahedral fields [26, 27]. As the crystal-field strength κ increases, the rotor states become gradually hindered and the rotational density distribution is more and more bound to the vicinity of the preferred crystallographic directions. Correspondingly, the rotational energies decrease below the potential barriers (zero of the potential energy) with the energy levels arranging in manifolds of rather high degeneracy. The lowest sixfold librational manifold of energetically close states forms at $\kappa \gtrsim 15$, composed of $A_{1g}(1)$, $T_{1u}(3)$, and $E_g(2)$ irreducible representations (degeneracies in parentheses). The first excited, twelvefold, librational manifold becomes bound for $\kappa \gtrsim 55$, where the energy gap to the lower set of levels is about 25. The ground and excited sets of levels correlate to the $J = 0$–2 and $J = 2$–4 free-rotor states, respectively. The sets of grouped states bound to small-angle libration are nominated as tunneling multiplets [24, 27], indicating very low transition frequencies among different members.

For a ready reference, we give the energy-level spectra $E_n(\kappa)$ with $\kappa = 25$ and $\kappa = 50$ up to the $n = 93$ state in Table I. The energies are utilized also in Sec. IV B for the analysis of the time-dependent alignment signals. For the weaker crystal-field strength, the potential yields a tunneling splitting of $\Delta E_t = 1.14$ within the lowest librational manifold of six states ($1A_{1g}$–$1E_g$). For the stronger crystal field we are closer to the librational limit and the tunneling splitting reduces to $\Delta E_t = 0.25$. The energetic gap to the first librationally excited manifold of states is found to be 13 or 24 ($1E_g$–$1T_{2g}$) for $\kappa = 25$ or $\kappa = 50$, respectively [27]. Only in the latter case, another distinct librational splitting of 13 ($1T_{1g}$–$2A_{1g}$) can be distinguished. The higher energy levels appear to be unstructured since much higher crystal-field strengths would be required to form librational manifolds. For the chosen $\mathcal{T} = 1$, the Boltzmann weight factors $w_n^{g/u}$ become $w_1^g = 0.322$, $w_{2,3,4}^u = 0.158$, and $w_{5,6}^g = 0.103$ at $\kappa = 25$, and $w_1^g = 0.196$, $w_{2,3,4}^u = 0.166$, and $w_{5,6}^g = 0.153$ at $\kappa = 50$. This is in contrast to the gas phase, where at this temperature mainly the ground ($|00\rangle$) state is populated ($w_0 = 0.705$).

B. Light–induced alignment

To give an idea of the rotational confinement with respect to the octahedral surrounding, we plot the rotational density of the ground (A_{1g}) state at $\kappa = 25$ in Fig. 1. For a few typical values of κ, we investigated in Refs. [26, 27] how the densities of the librational states can be manipulated by applying the external alignment field selectively with respect

7

TABLE I: The crystal-field energies $E_n(\kappa)$ scaled up by the ground-state energies, $E_1(\kappa = 25) = -7.7$ and $E_1(\kappa = 50) = -23.7$. The states are labelled according to their irreducible representations in the three point groups O_h, D_{4h}, and D_{2h} to facilitate relation with selection rules. Even (*gerade*) states are emphasized by bold numbers.

| $n(\kappa=25)$	$E_n - E_1$	O_h	D_{4h}	D_{2h}	$n(\kappa=50)$	$E_n - E_1$	O_h	D_{4h}	D_{2h}
1	**0.00**	A_{1g}	A_{1g}	A_{1g}	**1**	**0.00**	A_{1g}	A_{1g}	A_{1g}
2–4	0.71	T_{1u}	A_{2u}, E_u	B_{2u}, B_{1u}, B_{3u}	2–4	0.16	T_{1u}	A_{2u}, E_u	B_{2u}, B_{1u}, B_{3u}
5,6	**1.14**	E_g	A_{1g}, B_{1g}	A_{1g}, B_{2g}	**5,6**	**0.25**	E_g	A_{1g}, B_{1g}	A_{1g}, B_{2g}
7–9	**14.4**	T_{2g}	B_{2g}, E_g	A_{1g}, B_{1g}, B_{3g}	**7–9**	**23.8**	T_{2g}	B_{2g}, E_g	A_{1g}, B_{1g}, B_{3g}
10–12	16.4	T_{1u}	A_{2u}, E_u	B_{2u}, B_{1u}, B_{3u}	10–12	24.9	T_{1u}	A_{2u}, E_u	B_{2u}, B_{1u}, B_{3u}
13–15	17.1	T_{2u}	B_{2u}, E_u	A_{1u}, B_{1u}, B_{3u}	13–15	25.0	T_{2u}	B_{2u}, E_u	A_{1u}, B_{1u}, B_{3u}
16–18	**21.0**	T_{1g}	A_{2g}, E_g	B_{2g}, B_{1g}, B_{3g}	**16–18**	**26.5**	T_{1g}	A_{2g}, E_g	B_{2g}, B_{1g}, B_{3g}
19	**25.0**	A_{1g}	A_{1g}	A_{1g}	**19**	**39.1**	A_{1g}	A_{1g}	A_{1g}
20,21	**25.8**	E_g	A_{1g}, B_{1g}	A_{1g}, B_{2g}	**20,21**	**39.5**	E_g	A_{1g}, B_{1g}	A_{1g}, B_{2g}
22	30.3	A_{2u}	B_{1u}	B_{1u}	22–24	43.7	T_{1u}	A_{2u}, E_u	B_{2u}, B_{1u}, B_{3u}
23–25	32.5	T_{1u}	A_{2u}, E_u	B_{2u}, B_{1u}, B_{3u}	25–27	43.7	T_{2u}	B_{2u}, E_u	A_{1u}, B_{1u}, B_{3u}
26–28	32.7	T_{2u}	B_{2u}, E_u	A_{1u}, B_{1u}, B_{3u}	28	50.0	A_{2u}	B_{1u}	B_{1u}
29–31	**34.9**	T_{2g}	B_{2g}, E_g	A_{1g}, B_{1g}, B_{3g}	**29**	**51.5**	A_{2g}	B_{1g}	B_{1g}
32,33	40.5	E_u	A_{1u}, B_{1u}	A_{1u}, B_{2u}	**30,31**	**51.8**	E_g	A_{1g}, B_{1g}	A_{1g}, B_{2g}
34	**43.3**	A_{2g}	B_{1g}	B_{1g}	**32–34**	**52.5**	T_{2g}	B_{2g}, E_g	A_{1g}, B_{1g}, B_{3g}
35,36	**43.5**	E_g	A_{1g}, B_{1g}	A_{1g}, B_{2g}	35,36	54.4	E_u	A_{1u}, B_{1u}	A_{1u}, B_{2u}
37–39	**44.0**	T_{2g}	B_{2g}, E_g	A_{1g}, B_{1g}, B_{3g}	**37–39**	**55.3**	T_{2g}	B_{2g}, E_g	A_{1g}, B_{1g}, B_{3g}
40–42	45.6	T_{1u}	A_{2u}, E_u	B_{2u}, B_{1u}, B_{3u}	40–42	66.2	T_{2u}	B_{2u}, E_u	A_{1u}, B_{1u}, B_{3u}
43–45	**53.0**	T_{2g}	B_{2g}, E_g	A_{1g}, B_{1g}, B_{3g}	43–45	66.3	T_{1u}	A_{2u}, E_u	B_{2u}, B_{1u}, B_{3u}
46–48	**55.0**	T_{1g}	A_{2g}, E_g	B_{2g}, B_{1g}, B_{3g}	46–48	68.6	T_{1u}	A_{2u}, E_u	B_{2u}, B_{1u}, B_{3u}
49–51	57.0	T_{2u}	B_{2u}, E_u	A_{1u}, B_{1u}, B_{3u}	**49–51**	**72.3**	T_{2g}	B_{2g}, E_g	A_{1g}, B_{1g}, B_{3g}
52–54	57.2	T_{1u}	A_{2u}, E_u	B_{2u}, B_{1u}, B_{3u}	**52–54**	**74.8**	T_{1g}	A_{2g}, E_g	B_{2g}, B_{1g}, B_{3g}
55	**59.4**	A_{1g}	A_{1g}	A_{1g}	**55–57**	**81.0**	T_{1g}	A_{2g}, E_g	B_{2g}, B_{1g}, B_{3g}
56	65.8	A_{2u}	B_{1u}	B_{1u}	**58,59**	**81.3**	E_g	A_{1g}, B_{1g}	A_{1g}, B_{2g}
57–59	66.1	T_{2u}	B_{2u}, E_u	A_{1u}, B_{1u}, B_{3u}	**60**	**81.5**	A_{1g}	A_{1g}	A_{1g}
60,61	67.4	E_u	A_{1u}, B_{1u}	A_{1u}, B_{2u}	61–63	82.2	T_{2u}	B_{2u}, E_u	A_{1u}, B_{1u}, B_{3u}
62–64	71.2	T_{1u}	A_{2u}, E_u	B_{2u}, B_{1u}, B_{3u}	64	84.4	A_{2u}	B_{1u}	B_{1u}
65,66	**72.6**	E_g	A_{1g}, B_{1g}	A_{1g}, B_{2g}	**65**	**87.2**	A_{1g}	A_{1g}	A_{1g}
67–69	**72.6**	T_{1g}	A_{2g}, E_g	B_{2g}, B_{1g}, B_{3g}	66,67	87.4	E_u	A_{1u}, B_{1u}	A_{1u}, B_{2u}
70	**72.8**	A_{1g}	A_{1g}	A_{1g}	68–70	96.1	T_{1u}	A_{2u}, E_u	B_{2u}, B_{1u}, B_{3u}
71–73	**81.2**	T_{2g}	B_{2g}, E_g	A_{1g}, B_{1g}, B_{3g}	**71–73**	**97.7**	T_{2g}	B_{2g}, E_g	A_{1g}, B_{1g}, B_{3g}
74–76	**81.6**	T_{1g}	A_{2g}, E_g	B_{2g}, B_{1g}, B_{3g}	74–76	98.3	T_{2u}	B_{2u}, E_u	A_{1u}, B_{1u}, B_{3u}
77,78	**85.5**	E_g	A_{1g}, B_{1g}	A_{1g}, B_{2g}	77–79	98.5	T_{1u}	A_{2u}, E_u	B_{2u}, B_{1u}, B_{3u}
79–81	**86.5**	T_{2g}	B_{2g}, E_g	A_{1g}, B_{1g}, B_{3g}	**80–82**	**98.6**	T_{1g}	A_{2g}, E_g	B_{2g}, B_{1g}, B_{3g}
82–84	90.2	T_{2u}	B_{2u}, E_u	A_{1u}, B_{1u}, B_{3u}	**83,84**	**107.0**	E_g	A_{1g}, B_{1g}	A_{1g}, B_{2g}
85–87	90.3	T_{1u}	A_{2u}, E_u	B_{2u}, B_{1u}, B_{3u}	**85–87**	**111.4**	T_{2g}	B_{2g}, E_g	A_{1g}, B_{1g}, B_{3g}
88,89	98.5	E_u	A_{1u}, B_{1u}	A_{1u}, B_{2u}	88,89	114.0	E_u	A_{1u}, B_{1u}	A_{1u}, B_{2u}
90	98.5	A_{1u}	A_{1u}	A_{1u}	90	114.1	A_{1u}	A_{1u}	A_{1u}
91–93	98.5	T_{1u}	A_{2u}, E_u	B_{2u}, B_{1u}, B_{3u}	91–93	114.5	T_{1u}	A_{2u}, E_u	B_{2u}, B_{1u}, B_{3u}
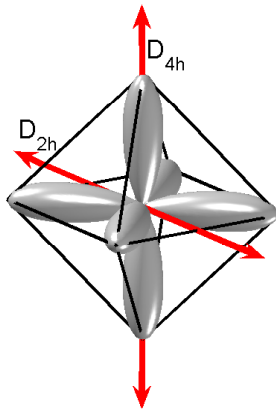
FIG. 1: (Color online) Rotational density of the ground librational (A_{1g}) state in the octahedral crystal potential at $\kappa = 25$. The lobes of the densities point towards the $\langle 100 \rangle$ crystallographic directions, i. e., towards the corners of the octahedron drawn around the density plot. The arrows represent the $\langle 100 \rangle$ and $\langle 110 \rangle$ polarization directions of the external alignment field. This reduces the total symmetry to D_{4h} or D_{2h}, respectively.

to the crystallographic directions. The vertical ($\langle 100 \rangle$) and horizontal ($\langle 110 \rangle$) two-headed arrows in Fig. 1 depict the applied directions of the alignment laser field. Correspondingly, the octahedral symmetry is reduced to that of the D_{4h} or D_{2h} point group, respectively. In the following, we shall use the nominations *cooperative* or *competitive* for situations where the polarization direction of the alignment field coincides with a crystal field minimum or a saddle point, respectively. High degrees of alignment can be achieved only for specific states and if the fields are cooperative. Otherwise, high efficiency of alignment mechanism is restricted to high field strengths and low temperatures [27].

We presented the dependence of the energy level spectra on the polarization direction and on the field strength $\Delta\omega$ in Refs. [26, 27] by solving the time-independent Schrödinger equation. The adiabatic eigenproperties of the total Hamiltonian were shown to result from direct and indirect alignment effects. In the former case, the field mixes suitable high-lying $|JM\rangle$ states into the state vector under consideration which becomes gradually squeezed along the field direction. In the latter case, perpendicular states are insensitive to the field but inherit alignment from higher parallel states of the same symmetry when they undergo an avoided crossing at relatively high values of $\Delta\omega$. The main features are reproduced in

Fig. 2. The crystal-field energy levels $E_n(\kappa)$ and the formation of librational multiplets (n = 1–6 and n = 7–18) is presented in panel (a). The small panel below (a) depicts the rotational density of ground A_{1g} state at $\kappa = 50$ in the spherical coordinates. Shown in the right-hand side of Fig. 2 are the energies $E_n(\Delta\omega; \kappa = 50)$ for A_{1g} states when the cooperative field (D_{4h}) is applied. The inserted density plots depict the light-induced alignment changes at the avoided crossing of $2A_{1g}$ and $3A_{1g}$ levels emphasized with circular symbols. The eigenenergy curves pertaining to Fig. 2 form the basis for the present time-dependent study, where a $\Delta\omega$ range is swept by a pulse. Our treatment includes the explicit time dependence of the alignment field intensity, and depending on the sweep rate, i. e., the pulse duration, the populations follow the eigenstates of the total Hamiltonian adiabatically or not, i. e., a rotational wave packet is formed. Following the usual separation made in gas phase reports, we divide our study of time-dependent alignment into nonadiabatic (Sec. IV) and adiabatic (Sec. V) cases.

IV.   NONADIABATIC ALIGNMENT OF LIBRATIONAL STATES

A.   Time–domain analysis

As a reference for our later work and to emphasize the importance of crystal-field effects, we first consider the case of gas phase molecules. To this end, time-dependent alignment with $\Delta\omega = 100$ for the coupling strength and $\mathcal{T} = 1$ for the temperature is studied. Figure 3 (left panel) shows the time-dependent alignment cosine $\langle\langle \cos^2\theta \rangle\rangle(\tau)$ in the regime of ultrashort alignment pulses with $\tau = 0$ corresponding to the center of the pulse. The FWHM is only a fraction of the time-scale unit $t_{\rm rot}$, and within the chosen σ range $(0.01$–$0.5)/\pi$, a rotationally broad wave packet is created and strongly nonadiabatic effects are observed. In particular, temporal oscillations of the post-pulse alignment are clearly present as alternation of dark and light regions. Note that alignment cosine values below the isotropic $1/3$ are given white color, see the lower half of the color bar.

The alignment pattern presented in the $\sigma\tau$-plane shows division into alternating high and low-contrast regions of σ. For example, cuts through $\sigma = 0.06$, 0.09, or 0.14 exhibit rather weak signal modulation as compared to cuts in between them. The trend strongly correlates with the wave-packet compositions created. Guided by the right panel of Fig. 3,
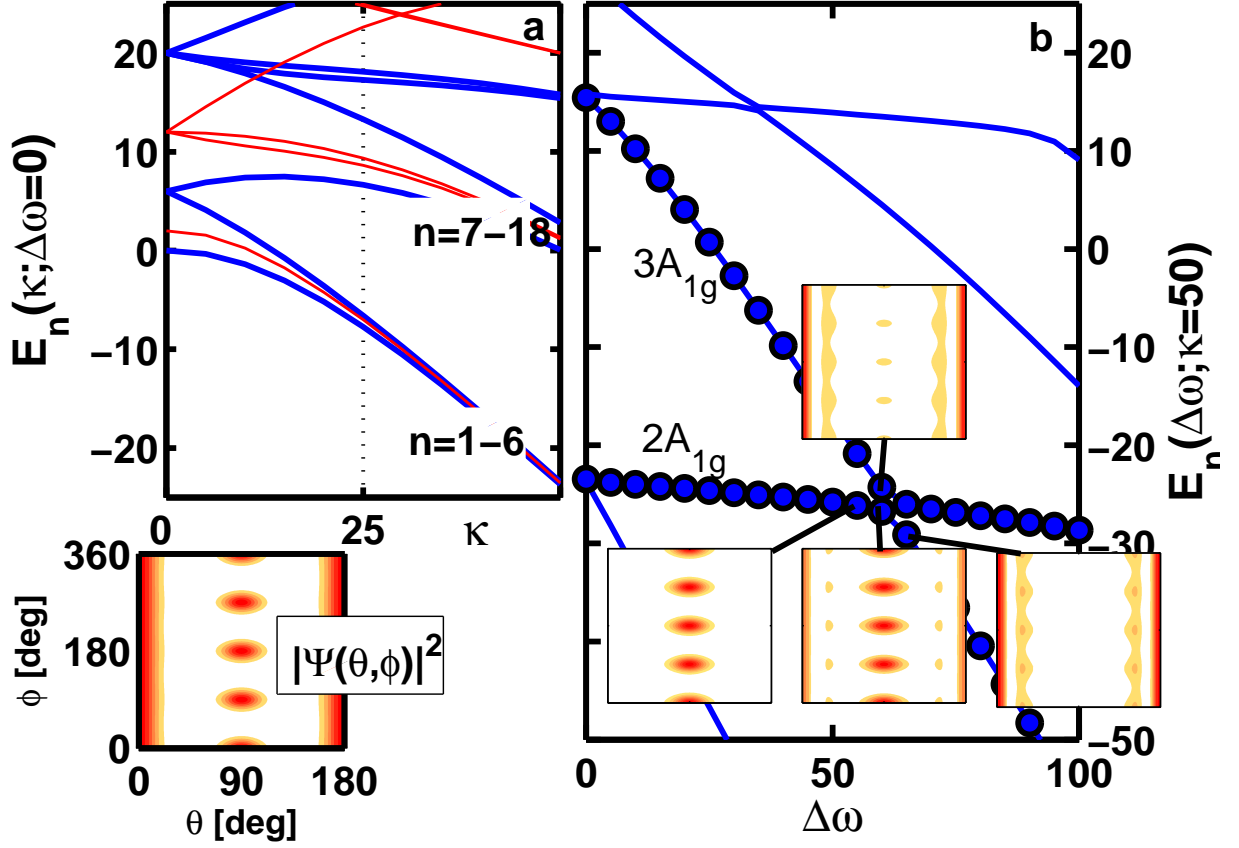
10

FIG. 2: (Color online) Energy level spectra pertaining to crystal-field states and light-induced alignment along a cooperative direction. (a) Correlation of the crystal-field energies between free rotor ($\kappa = 0$) and librational limits. Blue and red curves mark the gerade and ungerade states, respectively, and the grouping of states n into two librational manifolds is indicated. The contour plot below the panel displays the rotational density of the ground A_{1g} state at $\kappa = 50, \Delta\omega = 0$. (b) Dependence of the energy levels of $A_{1g}(D_{4h})$ symmetry on the alignment-field strength $\Delta\omega$. The $2A_{1g}$ and $3A_{1g}$ curves undergoing an avoided crossing are emphasized by circular symbols for the data points. Inserted in the panel, the corresponding densities are connected to the data points by lines: The $2A_{1g}$ density is given at $\Delta\omega = 55,60,65$ and the $3A_{1g}$ density is displayed for $\Delta\omega = 60$.

which exemplifies the degree of excitation in terms of expectation value $\langle \mathbf{J}^2 \rangle$ after the pulse, we concentrate on the $0.01 < \sigma < 0.05$ part in discussing the alignment in the following. The first peak with high alignment of the angular density along the polarization axis of the external field is found close to $\tau = 0$, i. e., while the pulse is still on but slightly retarded with
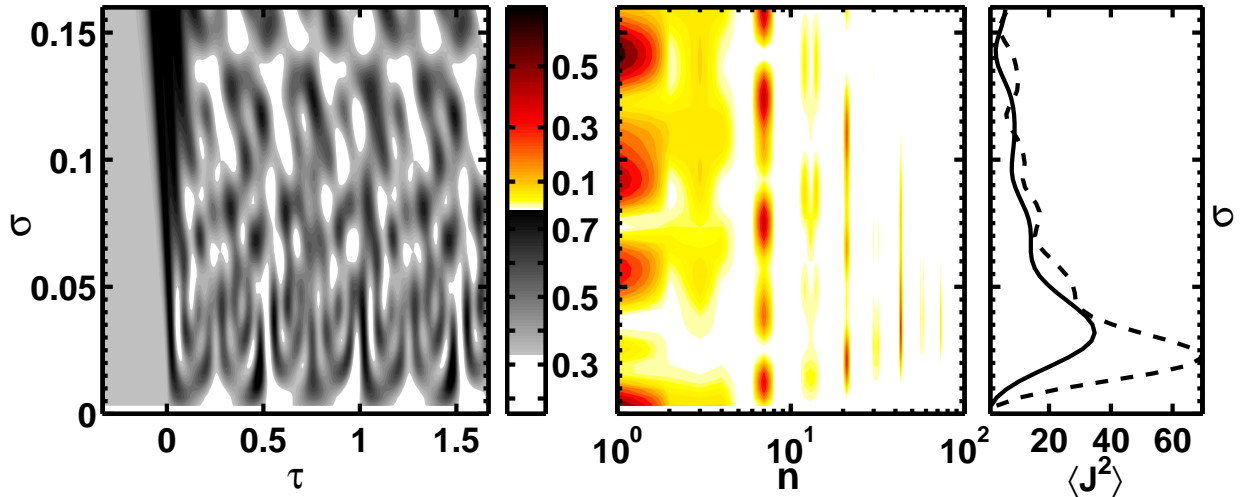
FIG. 3: (Color online) Dependence of time-dependent alignment cosine and wave-packet properties on the pulse width σ (FWHM) at $\mathcal{T} = 1$ in the gas phase. Left panel: Alignment cosine $\langle\langle\cos^2\theta\rangle\rangle(\tau)$ for $\Delta\omega = 100$, see lower half of the split color bar. Middle panel: Buildup of the wave packet for $\Delta\omega = 100$ in terms of occupation numbers $\sum_n w_n|C_{JM}^{(n)}|^2$ of free-rotor states $|J, M\rangle$, see upper half of the color bar. Right panel: Expectation value of the square of the angular momentum operator representing the degree of rotational excitation at $\Delta\omega = 100$ (solid) and $\Delta\omega = 200$ (dashed).

respect to the peak of the pulse. Values up to $\langle\langle\cos^2\theta\rangle\rangle \approx 0.8$ are reached within this σ range. After the laser pulse, the molecule is left in a coherent superposition of rotational states, and the time evolution of the wave packet exhibits recurrences in alignment. In particular, after t_{rot} ($\tau = 1$) the wave packet is again spatially aligned due to complete phase matching of the rotational components and the initial alignment peak is regained. In addition, a free molecule exhibits fractional rotational revivals as well. Half of the revival time, $t_{\mathrm{rot}}/2$ ($\tau = 1/2$), after the (retarded) first peak, the density is delocalized in perpendicular plane ($\langle\langle\cos^2\theta\rangle\rangle \approx 0.2$) with respect to the polarization of the field. This anti-alignment with tight angular width [13] is surrounded by two peaks with high parallel alignment (for $\sigma = 0.016$ even exceeding that of near $\tau = 0$), and the whole pattern is repeated at $3t_{\mathrm{rot}}/2$ as the coherence is maintained. Further oscillations in alignment signal function become washed out in thermal ensembles of gas-phase molecules [12, 13, 28] due to complex quantum beating and interference among the rotational wave packet. In summary, the simple relation for the spacing of the free-rotor energy levels of a linear gas-phase molecule (multiples of 2) leads to

the observation of the (fractional) revival intervals. However, this feature based on simple phase-matching condition is distorted as soon as spherical symmetry is violated, i. e., for nonlinear molecules [2].

The composition of the created post-pulse rotational density in terms of free-rotor states $|J, M\rangle$ at $\tau = \tau_f$,

$$|\Psi_n(\sigma, \tau_f)\rangle_{\text{gas}} = \sum_{JM} C_{JM}^{(n)}(\sigma, \tau_f)|J, M\rangle, \tag{7}$$

is given in terms of thermally averaged populations $\sum_n w_n |C_{JM}^{(n)}|^2$ in the middle panel of Fig. 3. Here τ_f denotes a time ($\tau \geq 2\sigma$) at which the field has decayed ($g(\tau_f) \leq 2^{-16}$) and the time evolution is determined by the energy phases of the $|J, M\rangle$ states solely. A logarithmic contour-level spacing has been used to resolve for low populations also ($\sum_n w_n |C_{JM}^{(n)}|^2 > 0.015$), see upper half of the color bar. In addition, the state label $n = (J + 1)^2 - J + M$ is plotted in log-scale to emphasize the population of low-energy states. The $\Delta J = \pm 2, \Delta M = 0$ selection rule for the second order molecule–light interaction of Eq. (4) determines the allowed transition routes from the initially dominant $|0, 0\rangle$ state. Hence, high populations are found for $|0, 0\rangle (n = 1)$, $|2, 0\rangle (n = 7)$, $|4, 0\rangle (n = 21)$, and $|6, 0\rangle (n = 43)$ states while odd J states are considerably less populated because of the lower initial population of the $|1, M\rangle$ states for the low temperature, $\mathcal{T} = 1$, considered here. For the shortest pulses applied, $\sigma < 0.01$, the low-amplitude alignment modulation shows only a single frequency with a period of $t_{\text{rot}}/3$, corresponding to the energy difference of $J = 0$ and $J = 2$ states [(71–63)% of population resides on these states for $\sigma = (0.01–0.03)/\pi$, respectively]. The curves in the right panel of Fig. 3 show that the excitation degree is limited by the interaction time and the intensity of the pulse. The peak of this measure is found at $\sigma = 0.10/\pi$ for $\Delta\omega = 100$ and at $\sigma = 0.07/\pi$ for $\Delta\omega = 200$. In the former case, the occupation order is $|6, 0\rangle$, $|2, 0\rangle$, $|4, 0\rangle$, $|8, 0\rangle$, $|3, \pm 1\rangle$, and $|5, \pm 1\rangle$, followed by the initial and other odd $|J, 0\rangle$ states. Minima of rotational excitation coincide with those σ values where most of the post-pulse population has remained in the $|0, 0\rangle$ state (see middle panel of Fig. 3) and where the alignment signal modulation is suppressed the most (see the left panel).

For a ready overview of time-dependent alignment of molecules trapped in a solid, we select four cases. Both the case of the polarization coinciding with minima of the crystal field (cooperative, D_{4h}) and saddle points of the crystal field (competitive, D_{2h}) are studied for two different crystal-field strengths $\kappa = 25$ and $\kappa = 50$. The ratio of the external and
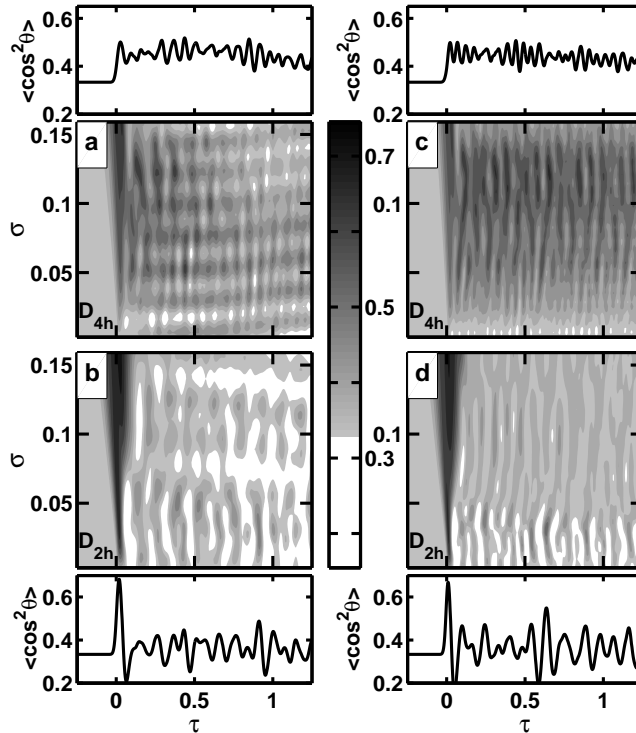
FIG. 4: Dependence of the time-dependent alignment cosine $\langle\langle\cos^2\theta\rangle\rangle(\tau)$ on the pulse width σ (FWHM) at $\mathcal{T}=1$ for molecules trapped in octahedral fields. Results are shown for cooperative (a,c) and competitive (b,d) polarization directions with D_{4h} and D_{2h} symmetries, respectively. The $(\Delta\omega,\kappa)$ parameters of the external and internal fields are (100,25) in the left panels (a,b) and (200,50) in the right panels (c,d). The alignment curves attached on top or below of the panels display the result for $\sigma=0.032$ in each of the cases.

internal field strengths is kept constant at $\Delta\omega/\kappa=4$, so that the excitation-field strength exceeds the barrier heights similarly in both cases. Each of the four $\langle\langle\cos^2\theta\rangle\rangle(\sigma,\tau)$ panels in Fig. 4 show similar graphical representations of the results as used above for the gas phase. In particular, panels (a,b) with $\Delta\omega=100$ are directly comparable to the left panel in Fig. 3. Post-pulse oscillations are present in all of the four cases considered here. As analyzed later on, this manifests the evolution of a rotational wave packet composed of crystal-field states, rather than free rotor states in the gas phase case. Adjacent to panels (a–d), we also plot representative cuts for the alignment at $\sigma=0.1/\pi$.

In the solid, a maximal value of ≈ 0.7 for the alignment cosine is reached, see the color

bar in Fig. 4. Comparing with the gas phase result it is $\approx 10\%$ lower due to different statistical weighting of the contributing states. Again, high peak of alignment occurs in all cases near the peak of the pulse. The alignment oscillations, resulting as the created superpositions of crystal-field states evolve after the pulse, are clearly distinct from the gas phase. In particular, the characteristic revival times for the gas phase are absent. Instead, the persistent interference pattern is the outcome of the highly irregular energy-level scheme of the trapped molecule, see Table I for E_n, and the initial populations ($n = 1$–6 occupied) in the thermal ensemble. The rapid modulation of the alignment measure in the crystal field thus substantially differs from the gas-phase result. Unexpectedly, the maximal alignment is higher in the competitive cases (b,d) than in the cooperative cases (a,c), especially for $\sigma < 0.05$. Noteworthy is also the different shape of the first alignment peak. For $\sigma > 0.05$ the competitive cases already resemble the adiabatic following, i. e., the alignment peak becomes symmetric, only slightly retarded with respect to $\tau = 0$, and the oscillation after the pulse is suppressed to a rather weak modulation. In the cooperative cases, the first peak is narrower and not so distinct from the further high-frequency oscillations that ride on a background leading to time-averaged alignment well above $1/3$. As explained below, qualitatively different excitation mechanisms govern the competitive cases (b) and (d) due to different selection rules. Most distinctly in Fig. 4, the time-averaged alignment values remain considerably lower than in the cooperative cases.

The direction dependent composition of the created post-pulse wave-packet state of crystal-field states $|n'\rangle$ at $\tau = \tau_f$,

$$|\Psi_n(\sigma, \tau_f)\rangle_{\text{solid}} = \sum_{n'} C_{n'}^{(n)}(\sigma, \tau_f)|n'\rangle \,, \tag{8}$$

is given in Fig. 5, again in terms of thermally averaged populations $\sum_n w_n |C_{n'}^{(n)}|^2$, for the same range of pulse widths σ as used in Fig. 4. We represent the colored contour level diagrams of $\sum_n w_n |C_{n'}^{(n)}|^2$ in a similar way as for the gas-phase result, see the middle panel of Fig. 3. On top of the panels (a–d) for populations, we also plot the corresponding crystal-field energies E_n to show the energy content of the excitation.

An understanding of the rotational excitation schemes and the resulting alignment can be achieved in terms of symmetry and selection rules. Upon interaction with the external laser field, the octahedral (O_h) symmetry of the internal (crystal) field is reduced to D_{4h} and D_{2h}, depending on the relative directions of external and internal fields, and only transitions
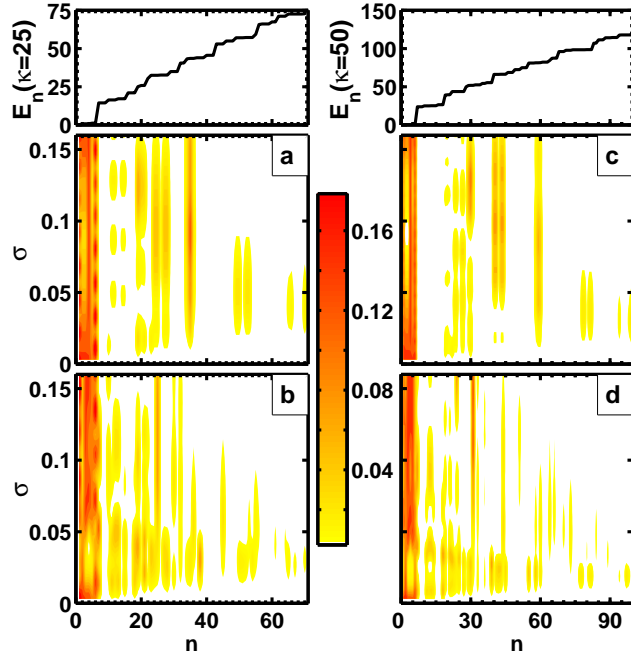
15

FIG. 5: (Color online) Crystal-field energies $E_n(\kappa = 25, 50)$ and corresponding post-pulse wave-packet populations: $|C_n|^2$ of the occupied crystal-field states $|n\rangle$ for pulse widths in the range $\sigma = (0.01\text{–}0.50)/\pi$. Labelling (a–d) as in Fig. 4. For a→b and c→d, the direction of the alignment-field polarization changes from cooperative to competitive. This leads to different occupations of the same crystal-field states.

within each of the irreducible representations of the subgroups are allowed. In particular, this also implies that the nonresonant alignment field conserves parity. For example, from the initially occupied states $n = 1$ and $n = 5\text{–}6$ transitions can only occur to gerade states, whereas states $n = 2\text{–}4$ can only mix with other ungerade states of the same symmetry. In the thermal average, both g-g and u-u combinations contribute to the observed alignment oscillations. Figure 5 represents the effect of selection rules in creating the wave packet. Differences in transition schemes for the same crystal field but for different polarizations can be seen by comparing the pairs (a) and (b) or (c) and (d). For example, the $n = 7$ state, which is the lowest state within the first librationally excited manifold, gains occupation from the initially occupied gerade states only in the competitive D_{2h} cases. This is because the state decomposes to $T_{2g}|B_{2g}, E_g|A_{1g}, B_{1g}, B_{3g}$ irreducible representations in the symmetry groups $O_h|D_{4h}|D_{2h}$, respectively. Using this notation, the relevant initial states (states n

= 2–4 are ungerade) are $A_{1g}|A_{1g}|A_{1g}$ for $n = 1$ and $E_g|A_{1g}, B_{1g}|A_{1g}, B_{2g}$ for $n = 5, 6$. The allowed transitions take place among the A_{1g} states in D_{2h}. We note that for both field directions there is also a significant coupling between the initially occupied $n = 1$ and $n = 6$ states corresponding to excitation of different tunneling states within the lowest librational multiplet.

Starting from the post-pulse wave packet of Eq. (8), the field-free evolution of the alignment signal $S(\tau) = \langle\langle\cos^2\theta\rangle\rangle(\tau)$ in terms of the crystal-field states is given by

$$
\begin{aligned}
S(\tau) &= \mathrm{Tr}\left\{\sum_n w_n \hat{\rho}_n(\tau)\cos^2\theta\right\} \\
&= \sum_{n,n'''} w_n \langle n'''|\Psi_n(\tau)\rangle\langle\Psi_n(\tau)|\cos^2\theta|n'''\rangle \\
&= \sum_{n,n'''} w_n \langle n'''|\sum_{n'} C_{n'}^{(n)}(\tau)|n'\rangle \sum_{n''} C_{n''}^{(n)*}(\tau)\langle n''|\cos^2\theta|n'''\rangle \\
&= \sum_{n,n',n''} w_n C_{n'}^{(n)}(\tau_f) C_{n''}^{(n)*}(\tau_f)\langle n''|\cos^2\theta|n'\rangle e^{-i\pi(E_{n'}-E_{n''})(\tau-\tau_f)} \\
&= \sum_{n'} A_{n'}(\tau_f) + \sum_{n'>n''} 2A_{n'n''}(\tau_f)\cos[\pi\Delta E_{n'n''}(\tau-\tau_f)],
\end{aligned}
\tag{9}
$$

where $A_{n'} = \sum_n w_n |C_{n'}^{(n)}(\tau_f)|^2 \langle n'|\cos^2\theta|n'\rangle$ expresses the time-independent part separated from the oscillating signal, with $A_{n'n''} = \sum_n w_n C_{n'}^{(n)}(\tau_f) C_{n''}^{(n)*}(\tau_f)\langle n''|\cos^2\theta|n'\rangle$ containing the coefficients and matrix elements corresponding to coupled pairs of states. The signal components oscillating at the energy differences $\Delta E_{n'n''}$ interfere and a beating pattern results with time scales inversely proportional to the energy level differences. In particular, two components evolve to a common phase $\pi\Delta E_{nn'}\tau = \pi\Delta E_{mm'}\tau \pm 2\pi p$ with a period $\tau_p = 2p/\Delta E_{nn',mm'}$, where $\Delta E_{nn',mm'} = \Delta E_{nn'} - \Delta E_{mm'}$ and p is an integer. For example, a free-rotor wave packet of $M = 0$, $J = 0, 1, 2, 3, 4, 5$ states would have $(J, J)'$ couplings $(0, 2)$, $(2, 4)$, $(1, 3)$, and $(3, 5)$ with transition energies 6, 14, 10, and 18, respectively. Then for the adjacent gerade–ungerade (J, J') pairs $(0, 2) - (1, 3)$, $(1, 3) - (2, 4)$, and $(2, 4) - (3, 5)$ the τ_p equals $2p/4$, i. e., $\tau_p = t_{\mathrm{rot}}/2 \times p$ including the half and full revivals discussed above. For the second nearest g–g or u–u pairs $(0, 2) - (2, 4)$ or $(1, 3) - (3, 5)$, the condition is $\tau_p = 2p/8 = t_{\mathrm{rot}}/4 \times p$, which includes the half and full revivals for even p. For the third nearest pair $(0, 2) - (3, 5)$, the condition $\tau_p = 2p/12$ prevails and the $t_{\mathrm{rot}}/2$ is met at $p = 3$. In other words, at half and full revivals all the free-rotor components are guaranteed to be in phase.

Similarly as in the gas phase case (see Fig. 3), the level of excitation becomes limited for long pulses, and high $n(J)$ levels corresponding to fast oscillations are found in the wave packet only up to $\sigma \approx 0.05$. In case (a) of Fig. 4 the rapid alignment oscillations are superimposed on a long-period ($\approx 2t_{\mathrm{rot}}$) background, which can be seen in the horizontal cut for $\sigma = 0.032$. This indicates the presence of a small splitting $\Delta E_{nn'}$. Instead of $\Delta E_{nn'} = 2$ of the free molecules, the smallest splitting here corresponds to the tunneling splitting within the initially populated librational manifold. One can expect dominant long periods in alignment recurrences especially for wave packets composed of low-$n(J)$ levels. This is indeed observed for the case presented in Fig. 4(a) in the impulsive region $\sigma \leq 0.02$ (the single-oscillation-frequency region in the gas phase), where the wave packet mainly consists of initial states with induced mixing between $n = 1$ and $n = 6$ (both A_{1g}). The same applies in principle for the competitive case (b) also, although the lower coupling strength by a factor of ten suppresses the effect. In case (c), the fields are twice as high and the tunneling splitting is about five times smaller. The corresponding period is even longer (not visible in the range of τ shown here) and therefore the time average of the presented alignment is high. A very long observation time is needed to resolve the effect in (d), where both the coupling strength and tunneling splitting are small. Vertical cuts through the alignment plots in Fig. 4 exhibit modulation at a given time elapsed, which reflects a different buildup of the wave packet. In particular, the broadness and the center of the wave packet shift upon lengthening the pulse as will be shown below.

B.   Energy–domain analysis

In this section we present an analysis of the time-dependent alignment in the energy/frequency domain. To this end, we perform Fourier transforms of the time series presented above. The power spectrum of the signal expression can be written as

$$P(E) \propto \left| \sum_{n'>n''} A_{n'n''} \int_{\tau_f}^{\tau_{\mathrm{max}}} \mathrm{e}^{-\mathrm{i}\pi E\tau} \cos[\pi \Delta E_{n'n''}(\tau - \tau_f)] \, \mathrm{d}\tau \right|^2 . \tag{10}$$

In the limit of $\tau_{\mathrm{max}} \to \infty$ this yields a set of delta distributions, located at the transition frequencies $\pi \Delta E_{nn'}$ present in the wave packet. Obviously, this spectrum can be used to learn the energies and corresponding intensities of transitions between the crystal-field states occupied by the pulse. Hence, the energy-level scheme of librational states in a crystal field
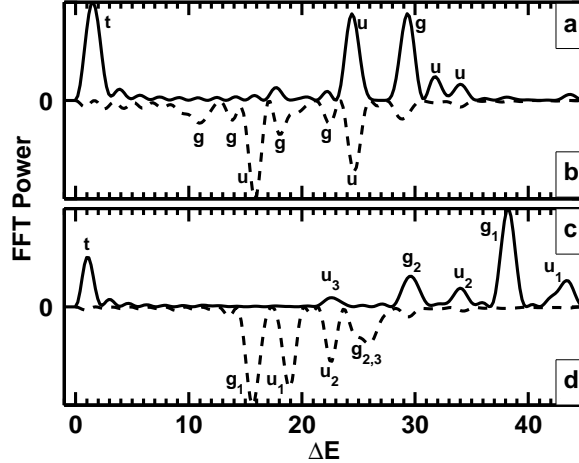
18

FIG. 6: Fourier transform power spectra of the time-dependent alignment signals of Fig. 4, for a short alignment pulse, $\sigma = 0.032$. Arrangement of panels (a–d) is adapted from Fig. 4 with negative sign (dashed lines) for competitive field directions in (b) and (d). The peaks can be assigned to energy differences ΔE among the states comprising the rotational wave packets evolving in the two crystal fields: $\kappa = 25$ for the upper panel and $\kappa = 50$ for the lower. The parity of the pairs of states involved in the transitions are indicated by g or u labels, respectively.

can be deduced to a certain extent from the observed modulation of a time-dependent alignment signal. This is manifest in Fig. 6, where we present the FFT power spectrum in energy scale ΔE for a single value of the pulse width, $\sigma = 0.032$ and for $\tau_{\max} = 1.25$. The cooperative (D_{4h}) and competitive (D_{2h}) pairs (a,b) and (c,d) from Fig. 4 are mirrored against each other to demonstrate the dependence on directionality of the alignment along the $\langle 100 \rangle$ and $\langle 110 \rangle$ crystallographic axes, respectively. With the help of the tabulated energy levels in Table I we can assign the peaks occurring in the Fourier transforms. This is alleviated by an inspection of the post-pulse wave function. Similarly as in Fig. 5, the significantly populated librational states are shown in Fig. 7 (here in linear scale).

Three main peaks are found in panel (a) of Fig. 6 for the cooperative case (D_{4h}). The most intense one of these at $\Delta E = 1.5$ and the one at 29.3 belong to gerade states, whereas the middle peak at $\Delta E = 24.5$ and the two satellites at 31.8 and 33.8 belong to ungerade states. From the tabulation of E_n in Table I we deduce the following assignments. Transition energies between states $n \leftrightarrow n' = (34, 35, 36) \leftrightarrow (65, 66, 70)$ cause the peak at $\Delta E = 29.3$.
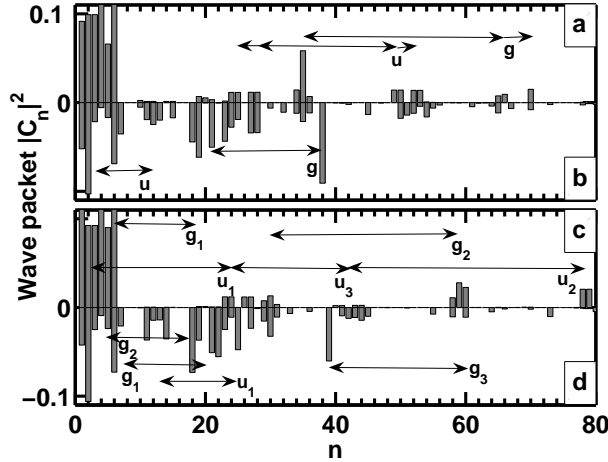
FIG. 7: Components of the post-pulse wave packet excited by an alignment pulse with $\sigma = 0.032$. Beatings between occupied levels of same symmetry generate the peaks found in frequency-domain representation of alignment signals. The arrows with g-u symbols indicate some of the assignments made in Fig. 6 with the help of energies E_n given in Table I. Panel labelling (a–d) as before.

The state $n = 35$ has the highest population after the initial states 1–6 as seen in Fig. 7, as well as in Fig. 5 for $\sigma = 0.032$. The equally intense, ungerade $\Delta E = 24.5$ peak can be traced back to the energy separation of levels $(24, 25, 27, 28) \leftrightarrow (49, 50, 52, 53)$. The tunneling splitting (labelled as t) between $n = 1$ and $n = 6$ manifests itself in the low-frequency peak at $\Delta E \approx 1$ corresponding to a period of $2t_{\mathrm{rot}}$. Upon extending the integration range to $\tau_{\mathrm{max}} = 3$, the tunneling peak becomes narrower and shifts from 1.5 to 1.1. We assign the lower-intensity satellites to transitions $(2–4) \leftrightarrow (23–25)$ for $\Delta E = 31.8$, and to transitions $(49, 50, 52, 53) \leftrightarrow (83–87)$ for $\Delta E = 33.8$.

The competitive case (D_{2h}) in this crystal field, panel (b) of Fig. 6, shows two main peaks at $\Delta E = 15.8$ and 24.6. Both belong to the ungerade progression, the latter being due to the same transition energies as in (a). As indicated in Fig. 7, the new peak at 15.8 is due to $(2–4) \leftrightarrow (10–12)$ couplings. Another difference to panel (a) is the presence of $T_{2g}|O_h$ components, especially intense for $n = 7$ and $n = 38$. Accordingly, the coupling $38 \leftrightarrow 21$ with $\Delta E = 18.2$ corresponds to the most intense gerade peak in the power spectrum, and also the coupling $7 \leftrightarrow 19$ with $\Delta E = 10.6$ is clearly visible. Only the longer simulation time can resolve a small feature close to $\Delta E = 1$ corresponding to tunneling.

Panel (c) of Fig. 6 contains the main peak g_1 at $\Delta E = 38.1$. We assign this to

20

(1,5,6)↔(19–21) transition energies. The other gerade peak g_2 at $\Delta E = 29.7$ originates more clearly from (29–31)↔(58–60) transitions. In addition, there is a $1 \leftrightarrow 30$ peak at $\Delta E = 51.8$ (outside the plot range). The ungerade peaks arise from the sequence: (2–4)↔(23,24,26,27) ↔(40,41,43,44)↔(78,79,81,82), for $u_1(43.4)$, $u_3(34.6)$, and $u_2(22.7)$, respectively. Due to the limited simulation time, the low-frequency peak indicative of tunneling splitting appears blue shifted. For longer simulation times this feature narrows and shifts toward zero: to 0.45 with $\tau_{max} = 3$ and to 0.28 with $\tau_{max} = 8$, which is necessary in order to cover the whole period. Longer simulation times also confirm the assignments of the broad peaks above as they split into narrow components, e. g., g_1 exhibits separated $1 \leftrightarrow 19$ and $1 \leftrightarrow 20$ transitions. Unfortunately, both gerade and ungerade states contribute to the low-frequency peak t (0.28 peak maximum and 0.44 peak shoulder, respectively), which excludes the assignment to pure ground state tunneling. A low-frequency modulation can occur accidentally from other closely separated states, such as those within the excited librational manifold, as well.

The first gerade peak g_1 in panel (d) at $\Delta E = 15.8$ originates from $7 \leftrightarrow (19, 21)$ transitions, whereas the broad structure with $\Delta E = 25.2$ and 26.2 consists of $5 \leftrightarrow 18$ and $39 \leftrightarrow 60$ transitions, respectively. The largest ungerade contribution u_1 at $\Delta E = 18.8$ is due to (11–14)↔(22–24,25,27) transitions. The other peak u_2 has the same origin as u_3 in panel (c).

In summary, notable qualitative differences have been found for cases (a–d). First of all, the different level spacings E_n for the two crystal fields with $\kappa = 25$ (a,b) and $\kappa = 50$ (c,d) lead to significant variations in the time-dependent signals and, hence, in the corresponding power spectra. In addition, upon changing the symmetry, e. g., from D_{4h} (a,c) to D_{2h} (b,d), by changing the polarization direction of the external field, complementary parts of the *same* librational spectrum become visible due to different selection rules. In addition, the composition of the post-pulse wave packet can be manipulated by the pulse duration. These aspects suggest a novel approach to the experimental determination of tunneling and librational energy levels of molecules in an octahedral field: By detecting the time-dependent, thermally averaged alignment signals $\langle\langle \cos^2 \theta \rangle\rangle(\tau)$ followed by a Fourier transform, transition energies can be resolved. In combination with model calculations such as those presented here, various models for the interaction with the internal field and/or their parameters (here the strength κ) can be distinguished. In particular for the shorter pulses investigated here, we have found that a very wide range of transitions becomes available by the nonresonant,

nonadiabatic pulses. Hence, time-dependent spectroscopy can be used to study spectral regions which would be hard to access otherwise, e. g., by conventional (CW) spectroscopy due to the inconvenient wavelengths [25]. In addition, the ultrafast alignment concept has recently been shown to provide a method for direct interrogation of dynamics and coherence spectroscopy in dissipative media [21, 22].

V. ADIABATIC ALIGNMENT CONTROL IN CRYSTAL FIELDS

In our previous reports [26, 27] we presented energy levels, wave functions, and (thermally averaged) expectation values of alignment (and orientation) for different field parameters. In particular, the latter were shown to depend not only on the field strength but also on the relative directions of internal (crystal) and external (laser) fields. Both in the cooperative and competitive case, intriguing flips of rotational density from horizontal (essentially unaligned) states to vertical (highly aligned) states were observed upon increasing the field strengths. They could be assigned to avoided crossings of energy levels $E_n(\kappa; \Delta\omega)$ of same symmetry states. Since those studies were conducted in a time-independent fashion, a dynamical interpretation of the behavior at these crossings had to be restricted to the adiabatic limit of infinitely long pulses.

In this section we address the case of pulses that are finite but long compared with typical time scales of the dynamical processes under investigation. For molecular alignment in the gas phase, the adiabatic regime is met when the pulse width is of the order of the rotational period and above. Assuming that the ratio of Rabi coupling and rotational energy determines the alignment degree during the pulse, Seideman [28] has found $\langle\cos^2\theta\rangle_{\max} \to 1 - \sqrt{1/\Delta\omega}$ for light molecules at low temperatures. A nontrivial question is the change of these aspects for rotational dynamics in a crystalline environment. First of all, we need to reformulate the adiabatic condition with respect to librational motion and tunneling. For the crystal-field strength $\kappa = 25$ chosen here, the tunneling frequency $\nu_t = \Delta E_t/h$ is roughly half the gas phase rotational frequency, see Table I. Hence, it is expected that twice as long pulses are needed to achieve fully adiabatic alignment. Since the tunneling frequency decreases as the crystal-field strength κ increases, even longer pulses are required to reach the adiabatic limit for $\kappa = 50$ with respect to tunneling dynamics. On the other hand, the opposite trend for the κ–dependence of the crystal-field splitting between librational manifolds suggests that

shorter pulses should suffice for an adiabatic condition with respect to libration, i. e., the hybridization of crystal-field states into an eigenstate of the total alignment Hamiltonian.

We compare the long-pulse alignment of a gas-phase molecule to the D_{4h} and D_{2h} symmetric solid-state cases in Fig. 8. The topmost panel for the gas phase reproduces the known result, that the pulse duration needs to satisfy the $\sigma \gtrsim 1$ condition for completely adiabatic evolution with only the $|0,0\rangle$ state populated at the end of the pulse [37], and compares well with Seideman's formula given above. For shorter pulses, $\sigma = 0.5$, also the $|2,0\rangle$ state becomes populated and the post-pulse evolution is governed by oscillations with a period of $\tau_p = 1/3$. The lower panels in Fig. 8 show that the pulse widths applied for the gas phase, σ = 0.5, 1, and 1.5, are too short to achieve adiabatic alignment in a crystal field with $\kappa = 25$. Even for $\sigma = 2$, the thermally averaged alignment degree exhibits large-amplitude post-pulse oscillation with a period of $1.75 t_{\text{rot}}$, see the D_{4h} panel (b). This is due to coherently coupled states $|1\rangle$ and $|6\rangle$ ($\tau_p = 2/\Delta E_{1,6} = 2/1.14 = 1.75$) that are populated in nonthermal manner at the end of the pulse. Hence, the rotational dynamics induced by a pulse with $\sigma = 2$ is adiabatic with respect to librational excitation but nonadiabatic with respect to transitions between the different tunneling states within a multiplet. Furthermore, inability to obtain fully adiabatic evolution manifests itself in the signal by the lack of symmetry with respect to $\tau = 0$. However, the post-pulse populations approach the thermal Boltzmann factors w_n as σ increases. For instance, in the D_{2h} panel (c) they are $|C_1|^2$ = 0.2501, 0.2970, 0.3093, 0.3158, 0.3206, and 0.3214 for σ = 0.5, 1, 1.5, 2, 3, and 4, respectively, for the lowest state ($w_1 = 0.3216$).

The remaining long-term modulation of the alignment signal is difficult to overcome, although smoother curves can be achieved for longer pulses as seen in Fig. 8 for $\sigma = 2$–4. The details, however, are not of main interest here. Actually, in a realistic experimental situation dissipation and/or dephasing due to contact with the surrounding crystal should serve to quench the remaining wave-packet coherence and corresponding oscillations in the signals. Therefore, in the following, we concentrate on the question of reaching high alignment during the pulse, which mainly depends on the intensity and polarization direction of the external field. Another feature of gas phase adiabatic alignment is that the maximum degree is achieved at the center of the pulse ($\tau = 0$). This property is also found for the case of matrix-isolated molecules, regardless of the pulse widths in the range of σ investigated here. Other significant differences between gas phase and octahedrally trapped molecules are
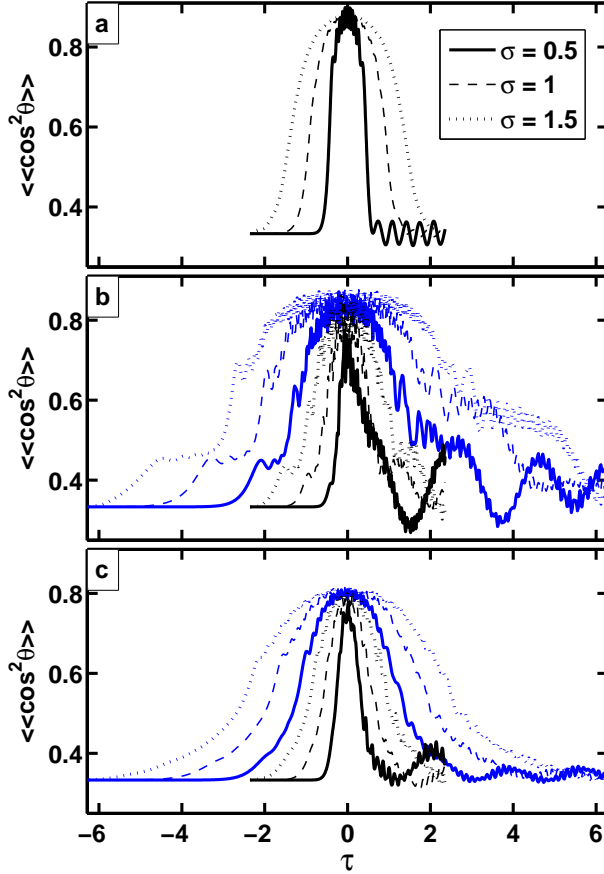
23

FIG. 8: (Color online) Near-adiabatic alignment $\langle\langle\cos^2\theta\rangle\rangle(\tau)$ with $\Delta\omega = 100$ at $\mathcal{T} = 1$ for (a) gas-phase molecule, (b) in the D_{4h} crystal field, and (c) in the D_{2h} alignment field. For the solid-state cases (b) and (c), $\kappa = 25$ and the pulse widths are (black) $\sigma = 0.5$ (solid), 1 (dashed), and 1.5 (dotted), and (blue) $\sigma = 2$ (solid), 3 (dashed), and 4 (dotted). For the gas phase (a), only $\sigma = 0.5$, 1, and 1.5 are applied.

apparent, however, depending on the alignment field direction with respect to the crystal. In panel (b) of Fig. 8, the alignment cosine increases in a stepwise manner. The same feature, although less markedly, is observed also in panel (c) for the D_{2h} case. These originate from the avoided crossings of the rotational energy levels in the combined (internal and external) fields, as will be analyzed below.

A. Cooperative fields

In this section we investigate the mechanism causing the stepwise progression of molecular alignment in octahedral fields during the first half of the pulse. To this end, we compare the signal in the cooperative case (D_{4h}) with stationary dressed-state energies $E_n(\Delta\omega)$ of Ref. [27]. Figure 9 presents a synopsis of the field intensity $\Delta\omega = 0$–100, avoided crossings of the energy levels E_n, and transient plateaus of the alignment degree $\langle\langle\cos^2\theta\rangle\rangle$ preceding the peak of the pulse. As indicated by the arrows in that figure, there are essentially three steps of enhancement: (1) The onset of alignment follows the initial mixing of $|1\rangle$ and $|6\rangle$ crystal-field states at $\Delta\omega \lesssim 5$ ($\tau \lesssim -2$) resulting in the formation of the $1A_{1g}$-$1A_{2u}$ pair of aligned states [27]. After this, the alignment is not enhanced but is subject to rather weak Stueckelberg oscillations which are a characteristic feature of population dynamics following nonadiabatic transitions. When the pulse intensity reaches the first avoided crossing at $\Delta\omega \approx 25$ (2), two of the remaining four perpendicular states (the doubly degenerate $1E_u$ state) flip along the field direction, and a shoulder feature is observed in the averaged signal. The mechanism consists of mixing the ($|3\rangle, |4\rangle$) crystal-field states (E_u) with librationally excited ones. The final increment (3) takes place after the pulse envelope has risen to the half-maximum at $\Delta\omega \approx 50$ ($\tau \approx -1$), i. e., exceeding the next avoided crossing region. There, the last two states of the (initially populated) ground librational manifold, $2A_{1g}$ and $1B_{1g}$, have turned into alignment, see also the inserted density plots of A_{1g} states in Fig. 2.

The maximum degree of alignment increases with the pulse duration σ. The values are between 0.78 and 0.88 for $\sigma = 0.5$–4, which is similar to the corresponding gas phase where $\langle\langle\cos^2\theta\rangle\rangle = 0.88$ for $\sigma = 2$. While only the $|0, 0\rangle$ state is significantly populated in the gas phase at $\mathcal{T} = 1$, in the crystal ($\kappa = 25$) all six states in the lowest librational manifold contribute. Remembering that the alignment is generally reduced at higher temperatures with wider population distributions [4, 9, 28, 37], $\langle\langle\cos^2\theta\rangle\rangle \approx 1 - \sqrt{\pi\mathcal{T}/\Delta\omega}(3/\mathcal{T} + 4)/8$ for $\mathcal{T} \gg 1$ in the gas phase [28], the high degree of alignment here manifests the cooperative nature of the interactions in the solid. While monotonic advancement of the alignment degree is tantamount to adiabatic alignment in the gas phase, here it is shown to proceed in a nonmonotonic way along the adiabatic states/levels. The remaining ripples around the peak of the pulse that result from the near-adiabatic condition do not significantly alter the alignment degree. High alignment ($> 70\%$) pertains during a period of $2t_{\rm rot}$, that is, during
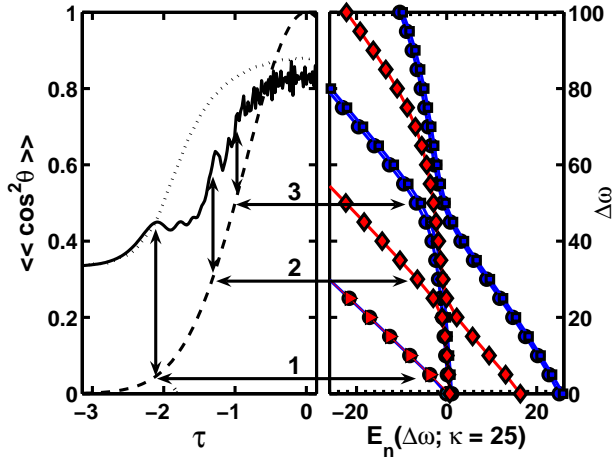
FIG. 9: (Color online) Left panel: Turn-on of the alignment in the crystal (solid curve) and in the gas phase (dotted curve) for $\sigma = 2$ pulse duration (dashed). Right panel: Adiabatic energy levels (from Ref. [27], and scaled as in Table I) for 1–$3A_{1g}$ (circles), $1A_{2u}$ (triangles), $1,2E_u$ (diamonds), and $1,2B_{1g}$ (squares) states in the D_{4h} symmetry. The instantaneous pulse intensity should be read from the right panel's $\Delta\omega$ axis. The enumerated arrows indicate the stepwise enhancement of alignment and its connection to the field-induced avoided crossings.

33 ps for a $B = 1$ cm^{-1} molecule.

B. Competitive fields

Next, we investigate the alignment control for a competitive arrangement of the two fields (D_{2h} symmetry). Here the target direction is along a $\langle 110 \rangle$ axis which corresponds to saddle points of the octahedral potential. Hence, the potential well induced by the laser field must be large compared to the static crystal field. We know from Ref. [27] that the required condition to turn the six populated states at $\mathcal{T} = 1$ into alignment is $\Delta\omega/\kappa \gtrsim 2$, as the avoided crossings occur at $\Delta\omega = 25$–30 (for $2A_{1g}$) and $\Delta\omega = 35$–40 (for B_{2u}) in the $\kappa = 25$ crystal field. The other four states exhibit rotational density lobes $45°$ off the target direction, and gradually become squeezed along the field direction as the pulse intensity rises. With only two out of six states undergoing avoided crossings, there are no visible plateaus but only slope changes in the rising alignment signal.

The effect of peak intensity on the alignment degree for the competitive (D_{2h}) case and for

TABLE II: Intensity dependence of the peak alignment degree $\langle\langle\cos^2\theta\rangle\rangle(\tau = 0)$ for $\sigma = 2$ pulse duration in the competitive (D_{2h} symmetry) and cooperative case (D_{4h}). Maximum degree of alignment ($\tau \neq 0$) is given in parentheses.

$\Delta\omega$	Gas phase	D_{4h}	D_{2h}	
		$\kappa = 25$	$\kappa = 25$	$\kappa = 50$
20			0.46 (0.46)	
30			0.51 (0.51)	
40			0.60 (0.60)	
50	0.83	0.74 (0.76)	0.64 (0.66)	0.43 (0.43)
60			0.68 (0.70)	
80			0.77 (0.77)	
100	0.88	0.81 (0.87)	0.79 (0.81)	0.58 (0.59)
200	0.91	0.87 (0.90)	0.86 (0.88)	0.77 (0.80)

$\sigma = 2$ is presented in the last two columns of Table II. The pulses exceed the above-mentioned condition of reaching the avoided crossings to a different degree. We apply the peak intensities $\Delta\omega = 20$, 30, 40, 50, 60, 80, 100, and 200 in the crystal field with $\kappa = 25$. In addition, we compute the alignment in a $\kappa = 50$ crystal for $\Delta\omega = 50$, 100, and 200 intensities. The alignment degrees are comparable for $(\Delta\omega, \kappa)$ pairs (20,25)↔(50,50), (40,25)↔(100,50), and (100,25)↔(200,50) as the ratios of the field strengths are approximately equal. The degree of alignment reflects the intensity-dependent weighting of insensitive states against those prone to alignment. All the components must be transformed, directly or via avoided crossings, parallel to the field direction in order to achieve high alignment values. Equivalently, the field-induced potential (V_α) must deform the crystal field (V_κ) such that no barrier exists in the total potential with respect to reorientation of the density along the target direction.

Because the pulses with $\sigma = 2$ are not yet fully in the adiabatic limit, the remaining nonadiabaticity gives rise to slight oscillations, and the maximum alignment can be instantaneously slightly larger than the value at $\tau = 0$. In the $\kappa = 25$, D_{2h} case, for example, the maximum of $\langle\langle\cos^2\theta\rangle\rangle(\Delta\omega = 200)$ is 0.88 instead of the peak value of 0.86. For the different $\Delta\omega$ values 50, 100, and 200, the stronger crystal field reduces the alignment by 33%, 27%, and 10% with respect to the weaker one. Comparison to the values in the cooperative (D_{4h})

and gas-phase cases also included in Table II further clarifies the competitive effect. The directional differences between the $\kappa = 25$ cases are 14%, 2%, and 1% for the same $\Delta\omega$'s as above. The reduction with respect to the gas phase amounts to 23%, 10%, and 5%, respectively. Thus the crystal-field effect is more pronounced for the low alignment-field strengths.

VI. CONCLUSIONS

We have numerically investigated the alignment of a linear molecule in a cubic crystal, where the trapping site of the molecule exhibits octahedral symmetry. This study serves to complement the previous reports [26, 27], where we have assessed the problem without explicit treatment of the time dependence and explained the solid-state effects using adiabatic field-dressed energy levels and corresponding librational wave functions only. Here, the alignment is obtained by intense nonresonant laser *pulses* which add an effective, time-dependent anisotropic potential to the molecule–solid system. In order to distinguish whether nonadiabatic or adiabatic progression of alignment prevails, the pulse duration has to be related to the time scales for tunneling and librational dynamics of the matrix-isolated molecules.

Long pulses approaching the adiabatic limit were used for obtaining high alignment degree during the pulse. A sufficient condition for control purposes is $\sigma = 1$, i. e., the pulse width is the rotational period of the free ground-state molecule. The corresponding alignment is relatively stable, although it does not originate from strictly adiabatic progression due to interfering tunneling states. By varying the polarization direction of the pulse with respect to the crystallographic axes, we can switch between cooperative and competitive effects of the superposed internal and external potentials. The alignment proceeds more gradually in the competitive case, since the avoided crossings in the thermal average are of lower importance. For both of the directions studied here, high alignment degrees close to the gas-phase results can be achieved.

In contrast to the adiabatic case, pulses, that are short with respect to oscillation periods of the lowest librational states, can be used to create nonstationary wave packets in the post-pulse regime. This gives rise to highly oscillating alignment signals which can be understood in terms of quantum beating of librational and other hindered-rotor states comprising the wave packet. Therefore, we propose to perform Fourier transforms of the observed alignment

modulation to analyze the energy level structure of a trapped molecule in a solid. To access various regions of the spectrum, different compositions of the wave packet can be controlled by varying the pulse parameters. The intensity and duration dictate to a large extent the transition cycles leading to the final wave packet. Furthermore, the polarization direction brings about different selection rules for the excitations, which can be used to select completely different states with otherwise identical pulses.

We note that throughout this work the ensemble average is calculated using the partition function from the field-free energies, i. e., the Boltzmann weight factors are computed from the crystal-field energies only. This is equivalent to assuming very long rotational re-equilibration times of the ensemble. However, as the energy gaps between aligned and perpendicular states become large in the external field, a thermalization during the pulse would lead to a sharper rise of alignment than presented here, since it is no more dictated by the avoided crossings. In addition, since the lattice is fixed against rearrangements of the constituent atoms, the tabulated threshold intensity values in pursuing adiabatic alignment should be considered as upper limits. While in the fixed lattice the time scales are a direct result of the energy level structure of the molecule in the solid, thermal effects of the environment need to be taken into account in the liquid phase. In computational studies it was found that the time needed to achieve alignment was in the order of rotational diffusion, as also stochastic rotational torque was generated by continuous collisions with the solvent [38]. This time scale can be much shorter than what is required for adiabatic alignment in the gas phase. However, fluctuations are much less important in cryogenic solids studied here. Intrigued by the recent dense media applications reported [21, 22], it will be interesting in our future work to proceed with molecules embedded in He droplets or bulk superfluid [39, 40, 41, 42].

---

[1] H. Stapelfeldt and T. Seideman, Rev. Mod. Phys. **75**, 543 (2003).

[2] T. Seideman and E. Hamilton, Adv. At. Mol. Opt. Phys. **52** (2005).

[3] B. Friedrich and D. Herschbach, Phys. Rev. Lett. **74**, 4623 (1995).

[4] B. Friedrich and D. Herschbach, J. Phys. Chem. **99**, 15686 (1995).

[5] T. Seideman, J. Chem. Phys. **103**, 7887 (1995).

[6] W. Kim and P. M. Felker, J. Chem. Phys. **104**, 1147 (1996).

[7] W. Kim and P. M. Felker, J. Chem. Phys. **108**, 6763 (1998).

[8] J. J. Larsen, K. Hald, N. Bjerre, H. Stapelfeldt, and T. Seideman, Phys. Rev. Lett. **85**, 2470 (2000).

[9] E. Péronne, M. D. Poulsen, H. Stapelfeldt, C. Z. Bisgaard, E. Hamilton, and T. Seideman, Phys. Rev. A **70**, 063410 (2004).

[10] E. Hamilton, T. Seideman, T. Ejdrup, M. D. Poulsen, C. Z. Bisgaard, S. S. Viftrup, and H. Stapelfeldt, Phys. Rev. A **72**, 043402 (2005).

[11] F. Rosca-Pruna and M. J. J. Vrakking, Phys. Rev. Lett. **87**, 153902 (2001).

[12] F. Rosca-Pruna and M. J. J. Vrakking, J. Chem. Phys. **116**, 6567 (2002).

[13] F. Rosca-Pruna and M. J. J. Vrakking, J. Chem. Phys. **116**, 6579 (2002).

[14] D. Daems, S. Guerin, E. Hertz, H. R. Jauslin, B. Lavorel, and O. Faucher, Phys. Rev. Lett. **95**, 063005 (2005).

[15] J. G. Underwood, B. J. Sussman, and A. Stolow, Phys. Rev. Lett. **94**, 143002 (2005).

[16] I. S. Averbukh and R. Arvieu, Phys. Rev. Lett. **87**, 163601 (2001).

[17] M. Leibscher, I. S. Averbukh, and H. Rabitz, Phys. Rev. Lett. **90**, 213001 (2003).

[18] C. Z. Bisgaard, M. D. Poulsen, E. Péronne, S. S. Viftrup, and H. Stapelfeldt, Phys. Rev. Lett. **92**, 173004 (2004).

[19] P. Marquetand, A. Materny, N. E. Henriksen, and V. Engel, J. Chem. Phys. **120**, 5871 (2004).

[20] J. Ortigoso, Phys. Rev. Lett. **93**, 073001 (2004).

[21] S. Ramakrishna and T. Seideman, Phys. Rev. Lett. **95**, 113001 (2005).

[22] S. Ramakrishna and T. Seideman, J. Chem. Phys. **122**, 084502 (2005).

[23] V. A. Apkarian and N. Schwentner, Chem. Rev. **99**, 1481 (1999).

[24] V. Narayanamurti and R. O. Pohl, Rev. Mod. Phys. **42**, 201 (1970).

[25] V. Berghof, M. Martins, B. Schmidt, and N. Schwentner, J. Chem. Phys. **116**, 9364 (2002).

[26] T. Kiljunen, B. Schmidt, and N. Schwentner, Phys. Rev. Lett. **94**, 123003 (2005).

[27] T. Kiljunen, B. Schmidt, and N. Schwentner, Phys. Rev. A (2005).

[28] T. Seideman, J. Chem. Phys. **115**, 5965 (2001).

[29] J. Manz, P. Saalfrank, and B. Schmidt, J. Chem. Soc. Faraday Trans. **93**, 957 (1997).

[30] B. Schmidt, Chem. Phys. Lett. **301**, 207 (1999).

[31] P. Žďánská, B. Schmidt, and P. Jungwirth, J. Chem. Phys. **110**, 6246 (1999).

[32] A. F. Devonshire, Proc. R. Soc. London, Ser. A **153**, 601 (1936).

[33] W. H. Flygare, J. Chem. Phys. **39**, 2263 (1963).

[34] H. U. Beyeler, J. Chem. Phys. **60**, 4123 (1974).

[35] C. J. Bradley and A. P. Cracknell, *The mathematical theory of symmetry in solids* (Clarendon, Oxford, 1972).

[36] B. Schmidt and P. Žďánská, Comput. Phys. Commun. **127**, 290 (2000).

[37] J. Ortigoso, M. Rodríguez, M. Gupta, and B. Friedrich, J. Chem. Phys. **110**, 3870 (1999).

[38] J. Ohkubo, T. Kato, H. Kono, and Y. Fujimura, J. Chem. Phys. **120**, 9123 (2004).

[39] L. Lehtovaara, T. Kiljunen, and J. Eloranta, J. Comput. Phys. **194**, 78 (2004).

[40] T. Kiljunen, L. Lehtovaara, H. Kunttu, and J. Eloranta, Phys. Rev. A **69**, 012506 (2004).

[41] J. Eloranta, H. Y. Seferyan, and V. A. Apkarian, Chem. Phys. Lett. **396**, 155 (2004).

[42] L. Lehtovaara and J. Eloranta, J. Low Temp. Phys. **138**, 91 (2005).